Vortices on a superconducting nanoshell: Phase diagram and dynamics

V. N. Gladilin,[1,2] J. Tempere,[1,3] I. F. Silvera,[3] J. T. Devreese,[1] and V. V. Moshchalkov[2]

[1]*TFVS, Universiteit Antwerpen, Groenenborgerlaan 171, 2020 Antwerpen, Belgium*
[2]*INPAC, K. U. Leuven, Celestijnenlaan 200 D, B-3001 Leuven, Belgium*
[3]*Lyman Laboratory of Physics, Harvard University, Cambridge, Massachusetts 02138, USA*
(Received 28 August 2007; published 14 January 2008)

In superconductors, the search for special vortex states such as giant vortices focuses on laterally confined or nanopatterned thin superconducting films, disks, rings, or polygons. We examine the possibility of realizing giant vortex states and states with nonuniform vorticity on a superconducting spherical nanoshell due to the interplay of the topology and the applied magnetic field. We derive the phase diagram and identify where, as a function of the applied magnetic field, the shell thickness, and the shell radius, these different vortex phases occur. Moreover, the curved geometry allows these states (or a vortex lattice) to coexist with a Meissner state, on the same curved film. We have examined the dynamics of the decay of giant vortices or states with nonuniform vorticity into a vortex lattice, when the magnetic field is adapted so that a phase boundary is crossed.

I. INTRODUCTION

Quantized vortices are a quintessential property of superfluids and superconductors. The energetically favored state when multiple quanta of vorticity are present is a lattice of singly quantized vortices. In ultracold Fermi gases, the recent observation of such a vortex lattice formed the "smoking gun" proof for superfluidity.[1] In nanoscopic superconducting samples, controlling the vortex behavior is essential for the development of new devices based on fluxon dynamics.[2] The confinement of Cooper pairs to length scales comparable to the correlation length also offers the prospect of probing fundamentally new phase topologies predicted by the theory, such as giant[3,4] and ringlike vortices.[5] This has led to renewed experimental efforts to observe giant vortex states, both in superconductors[6,7] and in superfluid atomic gases.[8]

In this contribution, we argue that superconducting spherical nanoshells form a promising candidate for realizing giant vortex states, and for engineering phase transitions between those states and a vortex lattice. Moreover, we show that nanoshells allow the coexistence of a Meissner state and a vortex state in equilibrium on one and the same superconducting film. Nanoshells are hybrid nanostructures consisting of a dielectric core (usually a silicon oxide nanograin), coated with a thin layer of metal.[9] When the metal in its bulk form is a superconductor, the nanoshell below the critical temperature will also exhibit superconductivity in the thin shell around the insulating core.

The superconducting order parameter in the nanoshell is well described by a macroscopic wave function $\psi = |\psi| e^{i\varphi}$ that obeys the coupled time-dependent Ginzburg-Landau (TDGL) equations. Vortices are characterized as topological defects in the phase φ (requiring a vanishing gap $|\psi|$). For thin shells, the description is simplified in two important ways. First, when the shell thickness is much smaller than the London penetration depth, the magnetic field will be only weakly perturbed by the nanoshell. Second, when the shell is thinner than the coherence length, the order parameter ψ will

not vary substantially in the radial direction in the shell; that is, ψ will depend only on the spherical angles $\Omega = \{\theta, \phi\}$. In the radial direction, ψ will be constant in the shell, and zero outside it. Note that confining ψ to the shell leads to an effective Ginzburg-Landau parameter κ that differs from its bulk value. In Sec. II we present the formalism, and in Sec. III the results, for thin shells. When the shell thickness is increased and becomes non-negligible with respect to the penetration depth, the magnetic field will be more strongly perturbed, and the field gradients affect the energetics. This case and the effect on the phase diagram are discussed in Sec. IV. Finally, we summarize the results for vortices in nanoshells in Sec. V.

II. GINZBURG-LANDAU FORMALISM ON THIN SHELLS

We assume that the shell is sufficiently thin for neglecting variations of the order parameter across the shell. In other words, the order parameter ψ will depend only on the spherical angles $\Omega = \{\theta, \phi\}$. We use the spherical coordinates r, θ, ϕ with the origin at the center of the sphere. The angle θ is counted from the z axis parallel to the external homogeneous magnetic field. As in Ref. 12, we will use dimensionless variables by expressing lengths in units of $\sqrt{2}\lambda$, magnetic fields in units of $\Phi_0/(4\pi\lambda^2)$, and the vector potential in units of $\Phi_0/(2\sqrt{2}\pi\lambda)$, where λ is the penetration depth, $\Phi_0 = h/(2e)$ is the magnetic flux quantum, h is the Planck constant, and e is the elementary charge. Thus, the dimensionless parameters R, W, and H are linked to the radius of the nanoshell $\mathcal{R}$, its thickness $\mathcal{W}$, and the applied magnetic field $\mathcal{H}$ by the expressions $R = \mathcal{R}/(\sqrt{2}\lambda)$, $W = \mathcal{W}/(\sqrt{2}\lambda)$, and $H = 4\pi\lambda^2\mathcal{H}/\Phi_0$, respectively.

In our numerical treatment of superconducting states on spherical shells we exploit the time-dependent Ginzburg-Landau equation, which is known to be a powerful tool for studying both the dynamic and static properties of superconductors. For the thin shell under consideration, the behavior of the order parameter in a fixed (or slowly varying) mag-

netic field can be described by the TDGL equation (see Refs. 10 and 11)

$$\frac{\partial \psi}{\partial \tau} = (\boldsymbol{\nabla}_\Omega - iR\mathbf{A})^2 \psi + 2(\kappa R)^2 \psi(1 - |\psi|^2), \tag{1}$$

where κ is the Ginzburg-Landau parameter, $\mathbf{A}$ is the (dimensionless) vector potential, and $\boldsymbol{\nabla}_\Omega = \mathbf{e}_\theta(\partial/\partial\theta) + \mathbf{e}_\phi \sin^{-1}(\theta) \times (\partial/\partial\phi)$. The dimensionless variable τ is linked to the time t by the relation $\tau = Dt/\mathcal{R}^2$, with D the normal-state diffusion constant.

The vector potential $\mathbf{A}$ can be represented as a sum of the contribution $\mathbf{A}_1$, related to supercurrents in the shell, and the contribution $\mathbf{A}_0$, which corresponds to the external magnetic field $\mathbf{H}$. The vector potential $\mathbf{A}_0$ is chosen in the form

$$\mathbf{A}_0 = \mathbf{e}_\phi \frac{Hr \sin\theta}{2}. \tag{2}$$

In the case of a constant applied magnetic field $\mathbf{H}$, with increasing τ the function ψ, given by Eq. (1), approaches one of the (meta)stable states of the system ($\partial\psi/\partial\tau \rightarrow 0$). The thermodynamically stable state is to be found by comparing the Gibbs free energy for different solutions. The difference in the Gibbs free energy between a superconducting state and the normal state at the same magnetic field is given by the equation

$$\Delta G = \frac{\Delta G_0}{4\pi\kappa^2} \int_0^{2\pi} d\phi \int_0^\pi d\theta (\mathbf{A}_1 \cdot \mathbf{j} - \kappa^2|\psi|^4), \tag{3}$$

where ΔG_0 corresponds to the superconducting state with no vortices at $H=0$, i.e., the Meissner state present on the complete surface. The dimensionless density of supercurrents is denoted by $\mathbf{j}$ and expressed in units of $\Phi_0 c/(8\sqrt{2}\pi^2\lambda^3)$.

In this section, the shell is assumed to be sufficiently thin in order to make negligible the magnetic fields induced by supercurrents. Correspondingly, we can neglect $\mathbf{A}_1$ as compared to $\mathbf{A}_0$. Then, as seen from Eqs. (1) and (2), two independent parameters, which govern the solution of Eq. (1), remain: (1) the dimensionless size of the nanoshell $\rho \equiv \kappa R = \mathcal{R}/(\sqrt{2}\xi)$, determined by the ratio of the shell radius $\mathcal{R}$ to the Ginzburg-Landau coherence length ξ, and (2) the parameter $\eta \equiv HR^2/2 = \pi\mathcal{H}\mathcal{R}^2/\Phi_0$, equal to the number of flux quanta of the applied field that pass through the equatorial plane of the sphere.

When the magnetic field is increased beyond a critical value (computed below), a first vortex appears for nanospheres with radius large enough to sustain the vortex core, as depicted in Fig. 1(a). Upon further increasing the magnetic field, more quanta of flux can penetrates the spherical surface. This can be accommodated in a variety of ways: for example, as a giant vortex carrying more than one quantum Φ_0, shown in Fig. 1(b). In this case, the angular momentum is uniform over the spherical surface. It is also possible to envisage states with nonuniform distributions of angular momentum: a value L_1 near the poles and a value L_2 in a band near the equator. Such states are characterized by a ringlike vortex separating the regions with different angular momentum, as illustrated in Fig. 1(c). Also, states that do not have
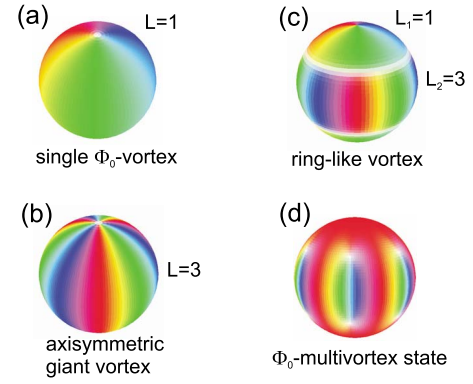

FIG. 1. (Color online) A few examples of vortex structures on a spherical shell are illustrated in this figure, to clarify the nomenclature used in the text. The amplitude and phase of the order parameter are shown as the saturation and hue of the color scale, respectively, in such a way that the vortex core region is white. (a) Shows a single Φ_0 vortex. In (b) a giant vortex (carrying multiple quanta of flux) is depicted. (c) Illustrates a ringlike vortex separating regions with different angular momentum. Finally, (d) shows the Φ_0-multivortex state, where an array of singly-quantized vortices is present.

axial symmetry should be investigated: we will show that these are in many cases the stablest state and that they then consist of an array of singly quantized vortices, illustrated in Fig. 1(d). Such states will be denoted as Φ_0-multivortex states, to emphasize that every vortex carries a single quantum of flux. In the next sections we start by investigating the axially symmetric states: giant vortices and ringlike vortices. Then, in the following section we investigate the condition under which those states decay into Φ_0-multivortex states, and the dynamics of this decay.

A. Giant vortex states

First, let us consider superconducting states, which keep the axial symmetry of the system, so that the order parameter ψ can be written in the form $\psi = f(\theta)\exp(iL\phi)$, where L has the sense of the winding number (vorticity). Then for a stationary distribution $f(\theta)$ the Ginzburg-Landau equation (1) reduces to the one-dimensional equation

$$\frac{\partial^2 f}{\partial\theta^2} + \cot\theta \frac{\partial f}{\partial\theta} - \left(\frac{L}{\sin\theta} - \eta\sin\theta\right)^2 f + 2\rho^2 f(1 - f^2) = 0 \tag{4}$$

with boundary conditions determined by the requirement that the θ component of the current density must be zero at the z axis: $\partial f/\partial\theta|_{\theta=0,\pi} = 0$. Solid lines in Fig. 2 illustrate typical behavior of the free-energy difference ΔG as a function of η for cylindrically symmetric states with different vorticity L. In the case of a thin spherical shell with $\rho=8$, as illustrated in Fig. 2, the value of L in the lowest cylindrically symmetric state increases with η from 0 at $\eta=0$ to 9 at $\eta=12.5$. The modulus f and phase $L\phi$ are illustated in Fig. 1(b), using the hue and saturation of the color scale, respectively. An increase of the applied magnetic field is seen to result also in a
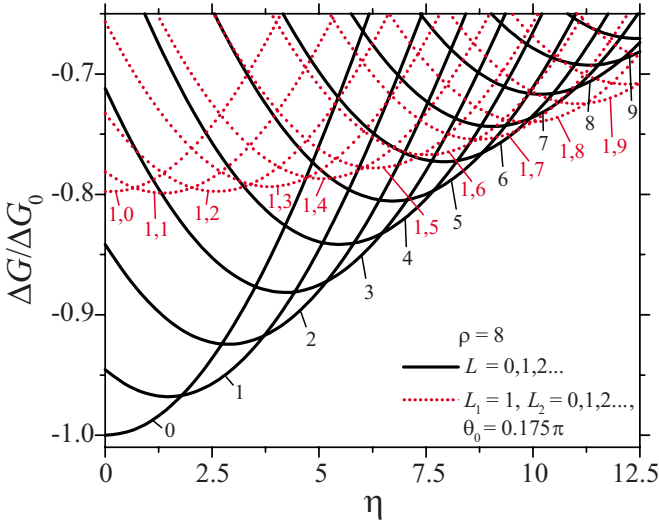
FIG. 2. (Color online) The free-energy difference is shown as a function of η, the number of flux quanta that pass through the equatorial plane of the sphere with radius $\rho=8$, for axially symmetric states. The black solid curves are for states with uniform vorticity (and a giant vortex). The red dotted lines are for states with ringlike vortices, characterized by the polar and equatorial angular momenta L_1 and L_2.

significant increase of the Gibbs free energy of the lowest state.

B. Ringlike vortices

In Ref. 12, when analyzing superconducting states in hollow cylinders, it was suggested that—under certain conditions—cylindrically symmetrical states with changing winding number can be more energetically favorable than the states with uniform L. Our calculations show that a similar situation occurs also in thin spherical shells with the dimensionless size larger than $\rho \approx 6$ (i.e., for $\mathcal{R} \gtrsim 8.5\xi$), but as we will show in the next section, such states decay into a lattice of singly quantized vortices breaking the cylindrical symmetry.

We have compared the Gibbs free energies for axially symmetric states with uniform winding number L and those for states where L_1, the winding number at $0 \leqslant \theta < \theta_0$ and $\pi - \theta_0 < \theta \leqslant \pi$, differs from L_2, the winding number at $\theta_0 < \theta < \pi - \theta_0$. The order parameter of the latter states on the sphere is illustrated in Fig. 1(c)—we will refer to such states as ringlike vortex states. The continuity of the order parameter as a function of θ requires vanishing $f(R,\theta)$ at the boundaries between regions with different winding numbers, i.e., at $\theta = \theta_0$ and $\pi - \theta_0$, as can be seen in Fig. 1(c). At sufficiently strong magnetic fields, the Gibbs free energy for states with ringlike vortices can become lower than that for states characterized by a unique winding number L over the whole θ range. This is illustrated by Fig. 2, where the dotted lines show the calculated free-energy difference $\Delta G(\eta)$ for states with $L_1=1$ and different L_2 on a shell with $\rho=8$ in the case of $\theta_0=0.175\pi$. It is worth mentioning that the values $\theta_0^{(min)}$, which minimize ΔG for the lowest ringlike vortex

state at a given η, are rather insensitive to the dimensionless nanoshell size ρ (at least, for $\rho \leqslant 10$). At the same time, the parameter $\theta_0^{(min)}$ is an increasing function of η. Thus, our calculations show that this parameter changes from $\theta_0^{(min)} \approx 0.12\pi$ to $\theta_0^{(min)} \approx 0.2\pi$ when η is increased from 7 to 15. However, moderate variations of θ_0 around $\theta_0^{(min)}$ only slightly affect ΔG for the lowest state with ringlike vortices. That is why in Fig. 2 we restricted ourselves to the case of a fixed value $\theta_0=0.175\pi$, which coincides with $\theta_0^{(min)}$ at $\eta = 10$.

In Fig. 2, the curve labeled 1,1 corresponds to the state with a ringlike vortex and uniform vorticity, which is qualitativley similar to the states analyzed in Ref. 5. The free energy of this state is always significantly higher than ΔG for the lowest giant vortex states with pointlike core. As can be further seen from Fig. 2, at $\eta \gtrsim 10$ the ringlike vortex states ($L_1 \neq L_2$) appear the most energetically favorable among the axially symmetric states. Thus, at $\eta \gtrsim 12.5$, the difference in $\Delta G/\Delta G_0$ between the state with $L=9$ and the state with $L_1 =1$, $L_2=9$ is larger than 0.025. At even larger values of η, states with three different regions of vorticity L_1, L_2, L_3 (characterized by two ringlike vortices) can become stable. However, our calculations show that in shells with $\eta \gtrsim 6$, where such ringlike vortices allow for decreasing the free energy of giant vortex states as compared to the case of a giant vortex, even lower values of ΔG can be achieved by breaking up the ringlike vortex (or vortices) into an array of singly quantized vortices. A natural question arises as to how stable are the aforedescribed giant vortex states with respect to decay into multiple singly quantized vortices. In order to answer this question, one has to return to the TDGL equation (1).

C. Numerical treatment

The finite-difference scheme, applied here to solve Eq. (1), is similar to that of Ref. 11, with necessary adaptations to the case of a spherical two-dimensional (2D) system. Two-dimensional grids, used in our calculations, typically have $\gtrsim 100$ equally spaced nodes in the θ interval from 0 to π and $\gtrsim 150$ equally spaced nodes in the ϕ interval from 0 to 2π. Cyclic boundary conditions for ψ are applied at $\phi=0$ and 2π. The boundary conditions at $\theta=0$ and π are determined by the requirement $\psi|_{\theta=0,\pi}=\text{const}(\phi)$. The step of the time variable τ is automatically adapted in the course of calculation. This adaptation is aimed to minimize the number of steps in τ, necessary for approaching a steady solution of Eq. (1), and—at the same time—to keep the solution procedure convergent. On average, the step in τ is $\sim 10^{-5}$ to $\sim 10^{-4}$ depending on the grid used as well as on ρ and η. When starting at $\tau=0$ from a random distribution of ψ (with $|\psi| \ll 1$), a (meta)stable solution of Eq. (1) is achieved typically at $\tau \lesssim 100$. When analyzing (meta)stability of states in a spherical shell, one has to keep in mind that a transition between states with different vorticity, in general, requires symmetry breaking. This means that simulations which assume a perfectly symmetric spherical nanoshell would tend to overestimate the stability of a state with respect to a possible transition to another state with lower free energy. In
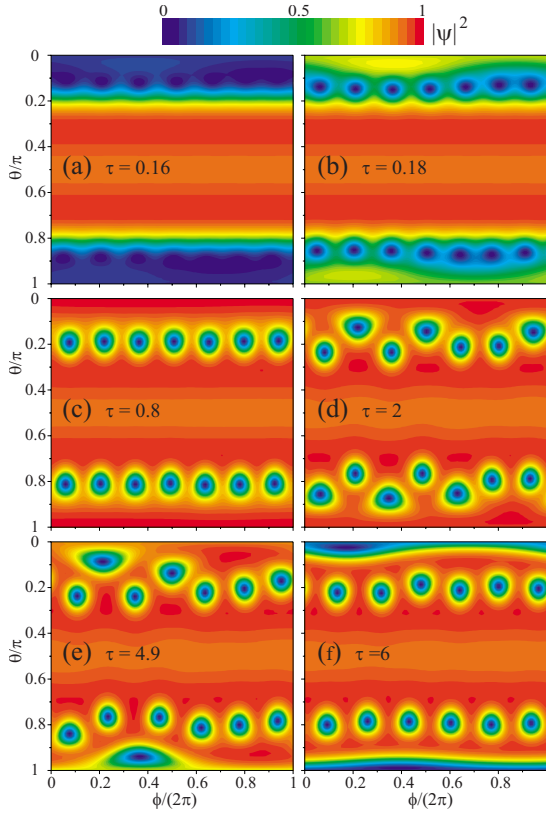
FIG. 3. (Color online) Evolution of the angular distribution of the squared modulus of the order parameter in a thin spherical superconducting shell with $\rho=8$ at $\eta=10$ in the case when the initial state (at $\tau=0$) is a giant vortex with $L=7$. Different panels correspond to different times τ. Note that for the purpose of illustration the normal region is now dark (blue), compared to white in Fig. 1.

order to model the effect of imperfections, inevitably present in realistic nanoshells, we consider spherical shells with small angular variations $\delta\rho(\theta,\phi)$ of the parameter ρ. Importantly, for relative magnitudes $|\delta\rho|/\rho$ ranging roughly from $\sim 10^{-8}$ to $\sim 10^{-3}$, the results of simulations do not depend in practice on a specific choice of the magnitude and distribution of these inhomogeneities. An appreciable effect of those imperfections on stable distributions of the order parameter appears only for $|\delta\rho|/\rho > 0.1$.

III. RESULTS AND DISCUSSION FOR THIN SHELLS

A. Decay of giant and ringlike vortices

In order to examine the stability of giant vortex states with respect to decay into multivortex states, we apply the computation scheme described in the previous section, starting at $\tau=0$ from a distribution of ψ that corresponds to a giant or ringlike vortex state. Typical examples of the evolution of the order parameter distributions are shown in Figs. 3 and 4 for the cases when the initial state is a giant vortex and a ringlike vortex, respectively. In the case of $\rho=8$ and $\eta=10$, the thermodynamically stable state corresponds to seven pairs of vortices with a single quantum Φ_0 of flux each, and it has a relative free energy $\Delta G/\Delta G_0 \approx -0.812$,
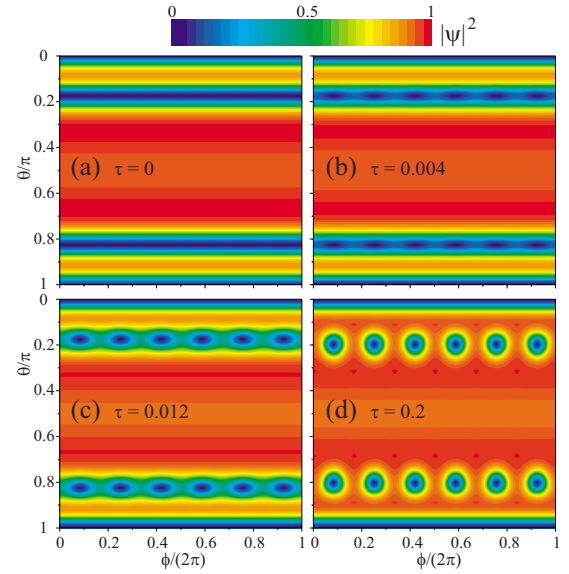

FIG. 4. (Color online) Evolution of the angular distribution of the squared modulus of the order parameter in a thin spherical superconducting shell with $\rho=8$ at $\eta=10$ in the case when the initial state (at $\tau=0$) is a ringlike vortex state with $L_1=1$ for $0 \leqslant \theta/\pi < 0.175$ and $0.825 < \theta/\pi \leqslant 1$; $L_2=7$ for $0.175 \leqslant \theta/\pi \leqslant 0.825$. Different panels correspond to different times τ.

approximately 0.07 lower than the value of $\Delta G/\Delta G_0$ for the lowest giant vortex state (see Fig. 2). Such lattices of vortices each with a single flux quantum Φ_0 will be denoted as Φ_0-multivortex states.

As illustrated by Figs. 3(a)–3(c), within a τ interval ~ 1 the initial giant vortex state with $L=7$ transforms into a chain of seven singly quantized vortices, which surround each pole of the sphere. In the course of the further rearrangement of the vortex pattern, one of the vortices moves to the pole, while the remaining six vortices tend to form a symmetric chain around the pole [see Figs. 3(d)–3(f)]. The free-energy gain due to this rearrangement is smaller by one order of magnitude than that due to the decay of the initial giant vortex into single vortices. Correspondingly, the τ interval necessary for this rearrangement appears to be relatively long: only at $\tau \approx 10$ does the solution reaches the equilibrium symmetric configuration of vortices (not shown in Fig. 3), similar to that found in Ref. 13, where Φ_0-multivortex states on a thin hollow sphere were studied in detail. As seen from Fig. 4, the transition from a ringlike vortex state ($L_1=1$ for $0 \leqslant \theta/\pi < 0.175$ and $0.825 < \theta/\pi \leqslant 1$; $L_2=7$ for $0.175 \leqslant \theta/\pi \leqslant 0.825$) to a Φ_0-multivortex state is even faster. The ringlike vortex core, which is present in the initial state [see Fig. 4(a)], decays into a chain of six single vortices very quickly: clear signatures of this decay can be found already at $\tau < 0.01$ [see Fig. 4(b)]. The equilibrium state with a vortex at the pole and six vortices symmetrically surrounding the pole is formed already at $\tau=0.2$.

The results of our calculations clearly indicate that giant and ringlike vortex states are rather unstable in spherical shells with relatively large ρ. This does not mean, however, that giant vortex states on a spherical shell are never stable. A decrease of the shell radius and/or an increase of the ap-
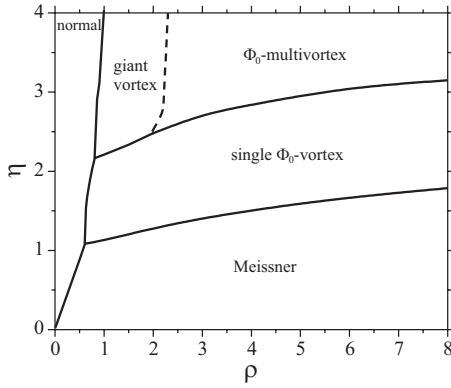
FIG. 5. Phase diagram for thin spherical superconducting shells in the (ρ, η) plane. The boundaries between the regions with the thermodynamically stable normal state, the Meissner state, the single Φ_0-vortex state, the giant vortex state, and Φ_0-multivortex states are shown by solid lines. The dashed line indicates approximately the boundary between the regions where giant vortex states or Φ_0-multivortex states are the thermodynamically stable states.

plied magnetic field enhance the role of the Lorenz forces, which act on the supercurrents and tend to drive vortices toward the poles of the shell. As a result, for sufficiently small ρ and sufficiently large η, the distance between vortex cores in a Φ_0-multivortex state becomes so small that physically a Φ_0-multivortex state appears indistinguishable from the corresponding giant vortex state. A similar continuous transition from a Φ_0-multivortex state to a giant vortex state with increasing magnetic field was recently found when solving the linearized Ginzburg-Landau equation for superconducting spherical grains.[14] Of course, in the case of such a continuous transition, the boundary between thermodynamically stable Φ_0-multivortex states and giant vortex states can be drawn only approximately. As the criterion of a transition from a multivortex state to a giant vortex state, here we have chosen the condition that the angular distance of vortex cores from the pole becomes smaller than $(10\rho)^{-1}$.

B. Phase diagram for thin shells

Our results, related to thermodynamically stable states on thin spherical shells are summarized in Fig. 5, where the solid lines indicate the boundaries of stability regions for the normal state, the superconducting Meissner states, single Φ_0-vortex states, giant vortex states, and Φ_0-multivortex states. The dashed line indicates the boundary between the regions, where giant vortex states (to the left of this line) or Φ_0-multivortex states (to the right of this line) are thermodynamically stable. As seen from Fig. 5, formation of vortices can be energetically advantageous only on sufficiently large shells: at $\rho \geqslant 0.63$ for states with $L=1$, at $\rho \geqslant 0.85$ for giant vortex states, and at $\rho \geqslant 1.95$ for Φ_0-multivortex states.

Within the region of the phase diagram where vorticity is present, we have made a subdivision into a region where there is a single, singly quantized vortex (indicated as "single Φ_0 vortex" in Fig. 5), and a region where more than one quantum of vorticity is present (indicated as "Φ_0 multivor-

tex" in Fig. 5). In principle, the latter region could be further subdivided into domains with 2,3,4,… quanta of vorticity. Rather than studying how many quanta are present, we focus on whether these quanta are coalesced into a giant vortex (left of the dashed line in Fig. 5), or whether they are present as an array of separate, singly quantized vortices in an Abrikosov lattice adapted to the spherical geometry (right of the dashed line in Fig. 5).

In the present analysis we are mainly interested in relatively small spherical shells, with radius comparable to the coherence length ξ. The phase boundaries for larger shells (with $\rho \gg 1$) can be estimated using, e.g., the analytical variational approach described in Ref. 15. Thus, the boundary between the thermodynamically stable Meissner and single Φ_0-vortex states in thin shells with $\rho \gg 1$ is approximately described by the expression $\eta = \gamma/2 + \ln(2\rho)/2$, where $\gamma \approx 0.5772$ is Euler's constant. The values of η given by this expression deviate from the corresponding numerical results by -23% at $\rho = 2$, by -6.3% at $\rho = 8$, and by -1.8% at $\rho = 300$. The boundary between the normal and superconducting states in thin spherical shells with $\rho \gg 1$ can be roughly approximated by the envelope function $\eta = 4\rho^2$.

While in Fig. 5 the phase diagram for thin spherical superconducting shells is shown in the (ρ, η) plane, it seems interesting to analyze the phase boundaries also in a more common form: in terms of the applied magnetic field $\mathcal{H}$ and the temperature T. We assume that the temperature dependence of the penetration depth λ is described by the empirical relation $\lambda(T) = \lambda(0)/\sqrt{1-(T/T_c)^4}$, while the (less important) temperature dependence of the Ginzburg-Landau parameter κ is roughly given by the expression $\kappa(T) = \kappa(0)/[1+(T/T_c)^2]$ (see, e.g., Ref. 16). In Fig. 6 we plot the phase boundaries for thermodynamically stable normal states, Meissner states, single Φ_0-vortex, giant vortex, and Φ_0-multivortex states on spherical superconducting shells with different radius $\mathcal{R}$, measured in units of the zero-temperature Ginzburg-Landau coherence length $\xi(0)$. As illustrated in Fig. 6(a), in the case, where the radius $\mathcal{R}$ is much larger than $\xi(0)$, giant vortex states are thermodynamically stable (at moderate applied magnetic fields) only in the close vicinity of the critical temperature T_c. With decreasing $\mathcal{R}$, the stability range of giant vortex states gradually extends toward lower temperatures and lower values of the magnetic flux through the shell. Correspondingly, in sufficiently small shells the stability range of Φ_0-multivortex states is restricted to a relatively narrow interval of $\mathcal{H}$ and to T, significantly lower than T_c [see Fig. 6(b)]. On even smaller shells [with $\mathcal{R}$ close to $\xi(0)$] no stable Φ_0-multivortex states are possible [see Fig. 6(c)]. For those small shells, the superconducting phase persists only for relatively weak (few Φ_0) magnetic fluxes through the shell. At the same time, as implied by a comparison between Figs. 6(b) and 6(c), the values of the applied magnetic field $\mathcal{H}$ that correspond to transitions with an increase of vorticity by 1 become significantly higher on decreasing the shell size.

IV. VORTEX STATES ON THICK SHELLS

A. Magnetization effects in thick shells

Now, let us extend our analysis to the case of relatively thick spherical shells, where magnetic fields, induced by su-
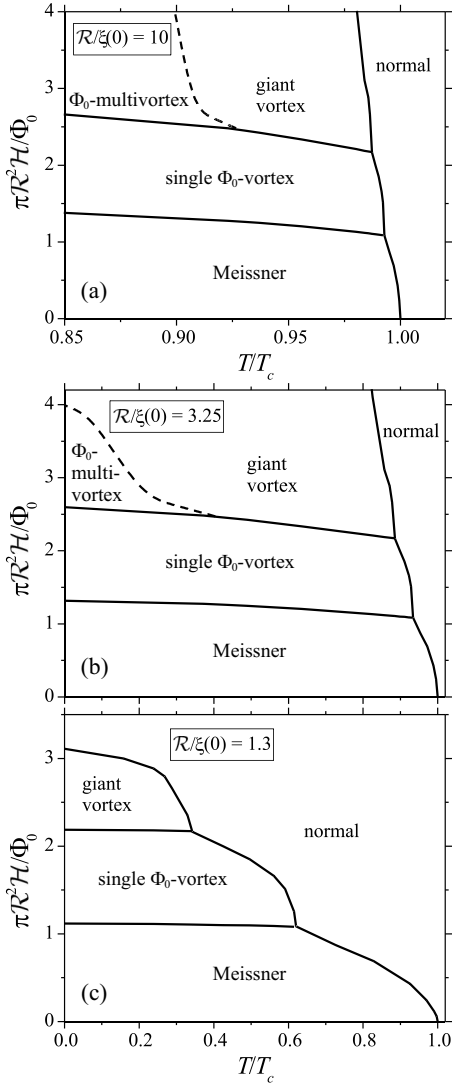
FIG. 6. Phase boundaries for thin spherical superconducting layers with different radius $\mathcal{R}$ as a function of the temperature T and the applied magnetic field $\mathcal{H}$. Boundaries between the thermodynamically stable normal state, Meissner state, single Φ_0-vortex state, giant vortex state, and Φ_0-multivortex state are shown by solid lines. The dashed line approximately indicates the boundary between the regions where giant vortex states or Φ_0-multivortex states are the thermodynamically stable states.

percurrents which flow in the shell, are non-negligible. At the same time, we assume that the thickness of the shell is still sufficiently small to allow neglect of variations of the order parameter ψ and of the vector potential $\mathbf{A}=\mathbf{A}_0+\mathbf{A}_1$ across the layer. For such a shell, currents across the layer can also be neglected. Expressing the vector potential $\mathbf{A}_1$ through the density of current $\mathbf{j}$ as

$$\mathbf{A}_1(\mathbf{r}) = \frac{1}{2\pi} \int d^3 r' \frac{\mathbf{j}(\mathbf{r}')}{|\mathbf{r} - \mathbf{r}'|}, \qquad (5)$$

the non-negligible components of the product $R\mathbf{A}_1$, which enters Eq. (1), can be written down in the following form:

$$RA_{1\theta} = \frac{WR}{2\sqrt{2}\pi} \int_0^\pi d\theta' \sin\theta' \int_0^{2\pi} d\phi' \{[\sin\theta \sin\theta'$$

$$+ \cos\theta \cos\theta' \cos(\phi-\phi')]Rj_{\theta'}(\theta',\phi')$$

$$+ \cos\theta \sin(\phi-\phi')Rj_{\phi'}(\theta',\phi')\}[1 - \cos\theta \cos\theta'$$

$$- \sin\theta \sin\theta' \cos(\phi-\phi')]^{-1/2}, \qquad (6)$$

$$RA_{1\phi} = \frac{WR}{2\sqrt{2}\pi} \int_0^\pi d\theta' \sin\theta' \int_0^{2\pi} d\phi' \{\cos\theta' \sin(\phi'-\phi)$$

$$\times Rj_{\theta'}(\theta',\phi') + \cos(\phi-\phi')Rj_{\phi'}(\theta',\phi')\}$$

$$\times [1 - \cos\theta \cos\theta' - \sin\theta \sin\theta' \cos(\phi-\phi')]^{-1/2}, \qquad (7)$$

where W is the dimensionless thickness of the shell. On the other hand, in the case of constant or slowly varying magnetic fields, using the relation

$$\mathbf{j} = \text{Re}\left[\psi^* \left(\frac{\boldsymbol{\nabla}}{i} - \mathbf{A} \right) \psi \right], \qquad (8)$$

the products Rj_θ and Rj_ϕ, which enter Eqs. (6) and (7), can be expressed through ψ, RA_θ, and RA_ϕ as

$$Rj_\theta = \text{Im}\left(\psi^* \frac{\partial \psi}{\partial \theta} \right) - RA_{1\theta}|\psi|^2, \qquad (9)$$

$$Rj_\phi = \frac{1}{\sin\theta} \text{Im}\left(\psi^* \frac{\partial \psi}{\partial \phi} \right) - (\eta \sin\theta + RA_{1\phi})|\psi|^2. \qquad (10)$$

In order to find the order parameter ψ and the corresponding vector potential, we solve self-consistently the set of equations (1), (6), and (7), using relations (9) and (10). From Eqs. (1), (6), (7), (9), and (10), one can see that for the relatively thick shells under consideration a set of independent parameters, which govern the solution, can be chosen as η, ρ, and ω, where the introduced additional parameter $\omega \equiv WR = \mathcal{WR}/(2\lambda^2)$ is linearly proportional to the thickness of the nanoshell and to its radius.

Figure 7 gives a few examples of magnetic field distributions, which correspond to thermodynamically stable states in spherical shells with $\rho=8$, $\omega=30$ and $\rho=8$, $\omega=10$. The patterns of magnetic field lines displayed in Fig. 7 are plotted for the particular case of the Ginzburg-Landau parameter $\kappa =0.8$, the (mean) dimensionless radius of the shell $R=10$, and the dimensionless thickness $W=3$ and 1. In general, none of the three mutually orthogonal components of the magnetic field $\mathbf{B}=\boldsymbol{\nabla}\times\mathbf{A}$ is zero, so that the field lines are three dimensional. In Fig. 7, however, we restrict ourselves to field-line patterns within symmetry planes, where the field lines are flat. As seen from Fig. 7(a), even in the case of a relatively thick shell ($W=3$) the magnetic fields, induced by the supercurrents in the Meissner state, are not sufficient for complete screening of the applied magnetic field inside the shell. Nevertheless, not only in the case of $W=3$ but also for a significantly thinner shell with $W=1$ [Fig. 7(b)], the net field inside the shell is much weaker than H. In the case of the state with $L=1$, the magnetic flux captured by a vortex pair is seen as
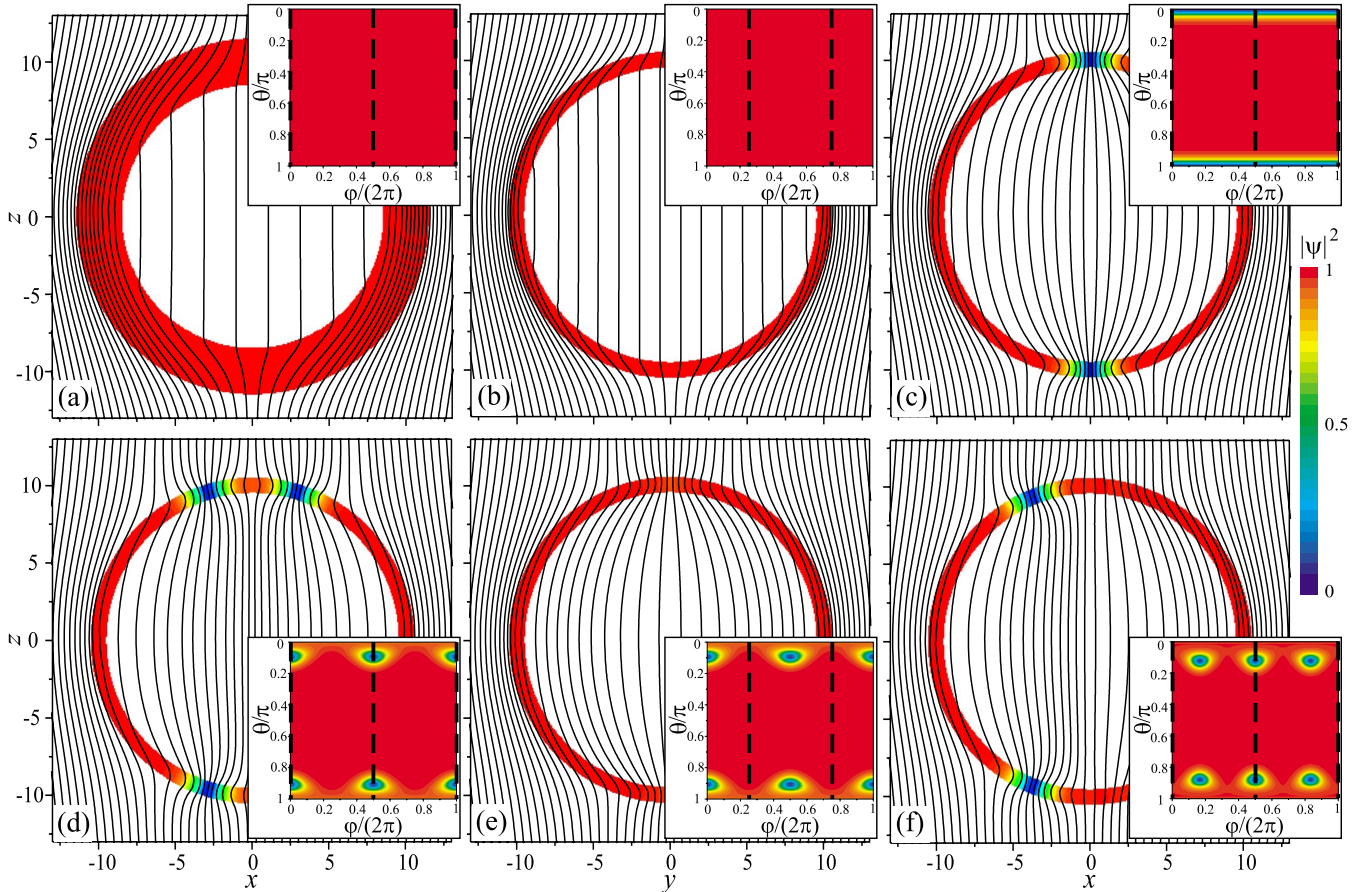
FIG. 7. (Color online) Magnetic field lines and distribution of the squared modulus of the order parameter for thermodynamically stable states in superconducting spherical shells with $\kappa=0.8$, $R=10$, $W=3$ (a) and $\kappa=0.8$, $R=10$, $W=1$ (b)–(f). The results are shown for the xz cross-section (a), (c), (d), and (f) and the yz cross-section (b) and (e) of the shell for different values of the parameter η and vorticity L: $\eta=5$, $L=0$ (a) and (b), $\eta=6.5$, $L=1$ (c), $\eta=8$, $L=2$ (d) and (e), $\eta=9.5$, $L=3$ (f). Insets: angular distributions of the squared modulus of the order parameter for the same values of η and the other parameters. Vertical dashed lines on each inset correspond to the cross section displayed on the main panel.

an increased density of field lines at the poles of the sphere [Fig. 7(c)]. At the same time, in the depth of the sphere the magnetic field is relatively homogeneous, only slightly increasing toward the z axis. Also for states with higher vorticity, a considerable local increase of the magnetic-flux density takes place only at the vortex cores within the superconducting shell, while in the depth of the sphere the density of magnetic field lines is considerably more homogeneous [see Figs. 7(d)–7(f)].

B. Phase diagram for thick shells

As seen from Fig. 7, the magnetic fields induced by supercurrents can be considerably large even for shells with quite moderate thickness ($W \sim 1$). These fields strongly affect the stability range for superconducting states with different vorticity in a spherical shell. In Fig. 8, we present the calculated phase diagram for relatively thick spherical shells with $\omega=10$. As follows from a comparison of Fig. 8 to Fig. 5, an increase of the thickness of a spherical shell results in a well-pronounced shift of the boundaries between states with different vorticity toward higher magnetic fields η. In par-

ticular, for $\rho>0.8$, the range of η where Meissner states are thermodynamically stable is more than two times wider in the case of $\omega=10$ as compared to the case of $\omega\rightarrow0$. One can also see that for a relatively thick spherical shell ($\omega=10$) the boundary between giant vortex and Φ_0-multivortex states is shifted toward significantly larger values of ρ as compared to those in the case of $\omega\rightarrow0$. The increased stability of giant vortex states agrees with the results recently obtained by Baelus *et al.*[14] for the limit $W\rightarrow R$ of a full sphere, in the framework of linearized Ginzburg-Landau equations.

In Fig. 9 the phase boundaries for thermodynamically stable normal states, Meissner states, single Φ_0-vortex, giant vortex, and Φ_0-multivortex states are plotted in the $(T, \mathcal{H})$ plane. The results are shown for shells with different radius $\mathcal{R}$ and thickness $\mathcal{W}$. In order to keep the plots more universal, it is convenient to express the thickness in units of $\xi(0)\kappa^2(0)$. For thick nanoshells, there is a much more pronounced increase of the transition fields that correspond to a change of vorticity with lowering temperature [compare Figs. 9(a) and 9(c) to Figs. 6(a) and 9(c)]. When comparing Fig. 9(a) to Fig. 6(a) one can also see that with increasing nanoshell thickness the temperature range where giant vorti-
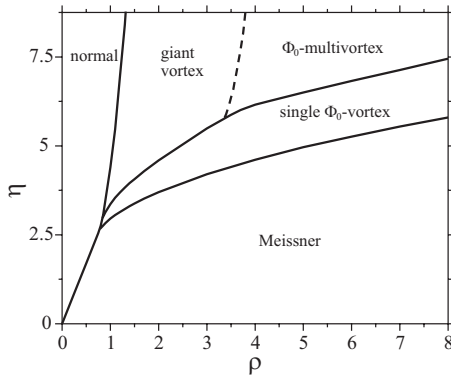
FIG. 8. Phase diagram for thick ($\omega = 10$) spherical superconducting shells in the (ρ, η) plane. The boundaries between the thermodynamically stable normal state, Meissner state, single Φ_0-vortex state, giant vortex state, and Φ_0-multivortex state are shown by solid lines. The dashed line approximately indicates the boundary between the regions where giant vortex states or Φ_0-multivortex state are the thermodynamically stable states.

ces are thermodynamically stable extends toward lower temperatures. With decreasing shell radius, this effect becomes quite pronounced even for relatively small values of $\mathcal{W}/[\xi(0)\kappa^2(0)]$ [compare Fig. 9(b) to Fig. 6(b)]. In sufficiently thick nanoshells, the temperature range where Φ_0-multivortex states are thermodynamically stable reduces to zero [see Fig. 9(c)], although in thin nanoshells of the same radius this range is relatively wide [see Fig. 6(b)]. Of course, when the temperature approaches T_c, the phase boundaries become almost insensitive to the value of $\mathcal{W}$. Indeed, at $T \rightarrow T_c$ the parameter ω always goes to zero [due to an increase of the penetration depth $\lambda(T)$], so that any nanoshell appears effectively thin.

V. CONCLUSIONS

Curving a superconducting film into a spherical shell changes its vortex-related properties drastically due to topological constraints.[17] The hairy-sphere theorem[18] is a straightforward example of such a constraint: it states that, in contrast to the situation on a flat film, there exists no nonvanishing continuous tangent vector field on the sphere. So every nonvanishing supercurrent velocity field requires discontinuities, such as vortices. The interplay between the Lorentz force due to an applied field and the vortex superflow will force these vortices away from the equator (leaving an equatorial "Meissner band") and toward the poles. This results in a "polar trapping potential," which is nearly quadratic near the poles. When vortices conglomerate at the poles, they may coalesce to form giant or ringlike vortices, and these dynamics and phases are the topic of the present paper.

Three contributions to the energy should be kept in mind to interpret the phase diagrams obtained in our calculations. First, to create a vortex, the kinetic energy of the associated supercurrent (on the 2D spherical surface) should be taken into account. This contribution increases when two vortices
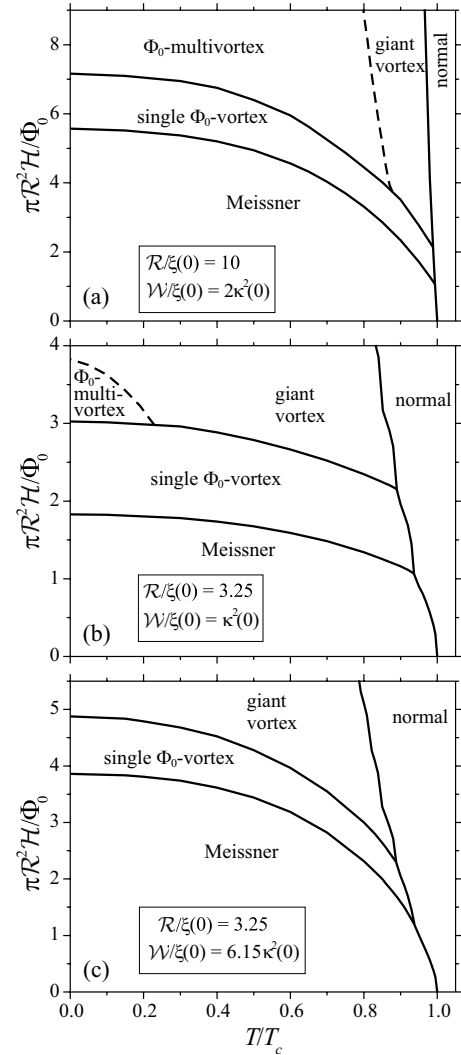

FIG. 9. Phase boundaries for spherical superconducting layers with different radius $\mathcal{R}$ and thickness $\mathcal{W}$ as a function of the temperature T and the applied magnetic field $\mathcal{H}$. The boundaries between the thermodynamically stable normal state, Meissner state, single Φ_0-vortex state, giant vortex state, and Φ_0-multivortex state are shown by solid lines. The dashed line approximately indicates the boundary between the regions where giant vortex states or Φ_0-multivortex states are the thermodynamically stable states.

with parallel vorticity are placed near each other, so it acts as a repulsion between the vortices. Thus, it tends to favor splitting of the giant vortices. Second, to create a vortex, the order parameter needs to be suppressed over a region typically of the size of the coherence length. The energy cost associated with this turns out to favor a multiply quantized (giant) vortex over the corresponding Φ_0-multivortex state. The energy cost is relatively larger for a smaller sphere, since proportionally a larger fraction of the total order parameter needs to be suppressed. The balance between these two energy contributions can be used to qualitatively understand the phase diagrams that we calculate for thin shells. Indeed, for magnetic fields corresponding to multiple quanta of vorticity, the smaller spheres will favor giant vortices, whereas the larger spheres favor the Φ_0-multivortex state. Note that this

contribution to the energy strongly disfavors ringlike vortex states.

The third contribution to the energy is related to the gradients in the magnetic field. When the shell is much thinner than the penetration depth, the currents on the shell will not substantially perturb the applied field, and this contribution plays no role. However, for thicker shells, this contribution does become important—as can be seen from Fig. 7, the magnetic field is substantially perturbed. When a Φ_0-multivortex lattice is present, the magnetic field flux is concentrated near each vortex core, and shielded in between, leading to a larger magnetic contribution to the energy than for a giant vortex. Thus, for a thick shell, this contribution will favor the giant vortex state. This agrees with our phase diagram showing that the region where the giant vortex is stable is growing for thicker shells.

The temperature dependence of the phase diagrams was studied straightforwardly by taking temperature into account through the Ginzburg-Landau parameters. When multiple quanta of vorticity are present, we find that the giant vortex phase forms the preferred high-temperature phase. This of-fers the prospect of probing a temperature-driven transition between a giant vortex and a Φ_0-multivortex state, alongside a magnetic-field-driven transition. Moreover, the vortex dynamics are shown to be insensitive to moderate imperfections in the shell; the energy contributions discussed here can overcome the pinning potential due to, for example, thickness inhomogeneities—such pinning potentials have in past experimental work hampered the detection of the giant vortex state. This robustness, together with the tunability of the phase diagram through a limited set of controllable parameters, makes superconducting nanoshells uniquely suited for the study of novel vortex states.

[1] M. W. Zwierlein, J. R. Abo-Shaeer, A. Schirotzek, C. H. Schunck, and W. Ketterle, Nature (London) **435**, 1047 (2005).

[2] V. V. Moshchalkov, L. Gielen, M. Dhallé, C. Van Haesendonck, and Y. Bruynseraede, Nature (London) **361**, 617 (1993).

[3] V. V. Moshchalkov, X. G. Qiu, and V. Bruyndoncx, Phys. Rev. B **55**, 11793 (1997).

[4] V. R. Misko, V. M. Fomin, J. T. Devreese, V. V. Moshchalkov, Phys. Rev. Lett. **90**, 147003 (2003).

[5] G. Stenuit, J. Govaerts, D. Bertrand, and O. van der Aa, Physica C **332**, 277 (2000); Phys. Lett. A **267**, 56 (2000).

[6] V. Bruyndoncx, J. G. Rodrigo, T. Puig, L. Van Look, V. V. Moshchalkov, and R. Jonckheere, Phys. Rev. B **60**, 4285 (1999); A. K. Geim, S. V. Dubonos, J. J. Palacios, I. V. Grigorieva, M. Henini, and J. J. Schermer, Phys. Rev. Lett. **85**, 1528 (2000); **86**, 1663(E) (2001); A. Kanda, B. J. Baelus, F. M. Peeters, K. Kadowaki, and Y. Ootuka, ibid. **93**, 257002 (2004).

[7] V. R. Misko, V. M. Fomin, and J. T. Devreese, Phys. Rev. B **64**, 014517 (2001).

[8] U. R. Fischer and G. Baym, Phys. Rev. Lett. **90**, 140402 (2003); P. Engels, I. Coddington, P. C. Haljan, V. Schweikhard, and E.

A. Cornell, ibid. **90**, 170405 (2003).

[9] R. D. Averitt, D. Sarkar, and N. J. Halas, Phys. Rev. Lett. **78**, 4217 (1997); S. J. Oldenburg, R. D. Averitt, S. L. Westcott, and N. J. Halas, Chem. Phys. Lett. **288**, 243 (1998).

[10] C. R. Hu and R. S. Thomson, Phys. Rev. B **6**, 110 (1972).

[11] R. Kato, Y. Enomoto, and S. Maekawa, Phys. Rev. B **44**, 6916 (1991).

[12] Hu Zhao, V. M. Fomin, J. T. Devreese, and V. V. Moshchalkov, Solid State Commun. **125**, 59 (2003).

[13] Q. Du and L. Ju, J. Comput. Phys. **201**, 511 (2004); Math. Comput. **74**, 1257 (2004).

[14] B. J. Baelus, D. Sun, and F. M. Peeters, Phys. Rev. B **75**, 174523 (2007).

[15] J. Tempere, V. N. Gladilin, I. F. Silvera, and J. T. Devreese, J. Low Temp. Phys. **148**, 181 (2007).

[16] M. Tinkham, Introduction to Superconductivity, 2nd ed. (McGraw-Hill, New York, 1996).

[17] J. Tempere, I. F. Silvera, and J. T. Devreese, Surf. Sci. Rep. **62**, 159 (2007).

[18] L. E. J. Brouwer, Math. Ann. **71**, 97 (1912).